High performance aluminum-air flow batteries through double-face architecture and laser-modified and friction-stir processed 3D anode

Lingyue Zhang [a], David Fieser [a], Bapi Bera [a], Douglas Aaron [a], Matthew M. Mench [a], Anming Hu [a,*], Yuan Li [b], Jian Chen [b], Zhili Feng [b], Antonino Gulino [c], Giuseppe Compagnini [c]

[a] Department of Mechanical, Aerospace and Biomedical Engineering, University of Tennessee, Knoxville, TN, 37996, USA
[b] Materials Science and Technology Division, Oak Ridge National Laboratory, Oak Ridge, TN, 37831, USA
[c] Chemistry Department, University of Catania, Viale A. Doria 6, Catania, 95125, Italy

HIGHLIGHTS

- Al-air batteries based on three-dimensional (3D) structured Al anodes.
- Periodic grooving for enhanced electrochemically active surface area (ECSA).
- Friction stirring for grain refinement and improved corrosion resistance.

ARTICLE INFO

ABSTRACT

Aluminum-air batteries (AAB) are regarded as one of the most promising beyond-lithium high-energy-density storage candidates. This paper introduces a three-dimensional (3D) Al 7075 anode enabled by femtosecond laser and friction-stir process which, along with a special double-face anode architecture provides world-class performance. Electrochemical characterizations prove that the corrosion resistance of the modified 3D Al 7075 FSP anode was enhanced, and electrochemically active surface area (ECSA) was increased compared with that of normal Al 7075 anode. Friction-stir processing reduced the mean grain size from 30 μm to 3 μm. The discharge performance of 3D Al 7075 FSP anode is shown to be quite stable, and the average values of energy density are significantly increased from 2256 mWh g^{-1} to 2941 mWh g^{-1} at 100 mA cm^{-2}. In a double-face flowing Al-air battery system, the 3D Al 7075 FSP anode exhibited significantly better electrocatalytic performance (discharge voltage of 0.76 V at 400 mA cm^{-2}, and power density of 337.8 mW cm^{-2}) than that of a commercial Al 7075 anode.

1. Introduction

Metal air cells have been highlighted as a next generation energy storage device, combining the possibilities of high energy density, low cost, environmental friendliness, and high inherent safety [1–5]. Aqueous aluminum–air batteries (AABs) are a promising candidate for efficient power delivery in the field of transportation and uninterrupted power supply due to a high theoretical energy density and specific capacity (8100 mWh g^{-1}, 2980 mAh g^{-1}, respectively), low density material (2.7 g cm^{-3}), rich abundance on earth, and cost-effectiveness [6–9]. Moreover, the major by-product after battery discharge is Al $(OH)_3$ or Al_2O_3, which is not only pollution-free but also recyclable

through industrial electrolysis processes [10]. Unfortunately, there are many choke points which hinder the commercialization of AABs, such as sluggish dynamics of oxygen reduction reaction (ORR), by-product deposition on the surface of the air cathode, high self-discharge rate, and low utilization of anodes [11–13]. These shortages limit the degree of accessible energy release for AABs so that the practical energy density only reaches 600–700 mWh g^{-1} [14,15].

Recently, the sluggish dynamics of oxygen reduction reaction have been mitigated by developing highly efficient catalysts [16–18]. Further, it has been shown that use of a flow cell design can avoid the issue of by-product deposition on the surface of the air cathode [19,20]. Moreover, after the oil displacement flow cell design was invented for

suppressing open-circuit corrosion during battery standby, the storage problem of flow cell battery was also eliminated [21]. However, to address issues such as the high self-discharge rate and low utilization of the anode, it is necessary to exploit highly efficient, corrosion-resistant Al anode materials and structures.

Currently, alloying Al with other elements (such as Zn, Mg, Sn, etc.) is still the most popular approach to retard Al anode corrosion in an alkaline electrolyte [22,23]. When these elements are incorporated into the aluminum matrix, the overall hydrogen evolution overpotential of aluminum alloys increases, inhibiting the hydrogen evolution corrosion reaction [24]. Grain refinement and homogenization of Al anodes has also been shown to be beneficial for improved corrosion resistance [25–27]. According to the work on friction-stir process for Al 7075 alloy grain refinement [28–30], the effect of grain size distribution on corrosion behavior is dependent on both the average grain size and the standard deviation in the grain size. However, although alloying these anti-corrosion elements and finer grain structures are indeed effective in resisting corrosion and increasing the specific capacity, they are also reduced in power and energy densities [31]. Furthermore, the achievable discharge current density for AAB is still limited as well.

More recent studies have shown that three-dimensional (3D) aluminum anodes are a promising development direction for AABs [32, 33]. 3D Al anodes with larger active surface area and operating current have potential to achieve high power density and energy density. Some researchers have investigated 3D-structured aluminum as the anode for AABs. For example, Yu et al. [34] employed 3D printed Al anode prepared by laser sintering. The cell constructed from laser sintered Al anodes provided 239 mAh g^{-1} discharge capacity at an operation voltage of 0.95 V at 0.5 mAcm^{-2}. Xu et al. [35] introduced spring-like aluminum anodes for flexible, wearable AABs with an energy density of 1168 mWh g^{-1} and a specific density of 935 mAh g^{-1} at 0.5 mAcm^{-2}. Zhang et al. [36] used aluminum mesh as the anode material for alkaline gel-electrolyte AABs based on polyacrylic acid, and exhibited a peak energy density of 1230 mWh g^{-1} at 18 mAcm^{-2} and peak power density of 91.13 mWcm^{-2} at around 1.3 V. Sha et al. [37] investigated the three-dimensional aluminum foam anode for alkaline Al-Air cells, concluding the peak power density of the 3D Al foam (80.6 mWcm^{-2}) increased by ~56.8 %, relative to the Al plate (51.2 mWcm^{-2}). Other studies with 3D structures anode [38–40] also proves that create 3D structures on surface of battery has been a new technology to improve the battery performances in recent years.

However, the discharge current density of most of the results are not high enough (less than 50 mAcm^{-2}), and this is because researchers utilized solid cell (i.e. closed) designs with the concomitant issue of by-product deposition on the surface of the air cathode. For high current density discharge research, most of them applied flow-electrolyte design (flow battery) to avoid this issue (for example, Liu et al. [13], Fu et al. [41] and Wen et al. [42] all use flow battery design and could reach the discharge current density as high as 100 mAcm^{-2}. Additionally, most previous research on 3D Al anodes focused on low current discharge performance, which is not suitable for many applications requiring a high-power density operation.

In this study, Al 7075 alloy was chosen as the base anode material because of the anti-corrosion elements it contains (Zn and Mg). A two-step, composite, controlled method - friction stir processing (FSPed) followed by femtosecond laser (fs laser) processing – was developed to prepare a novel, fine grain, 3D structured Al 7075 alloy as the anode of the AAB. Electrochemical characterization showed that the corrosion resistance and electrochemical properties of 3D structured Al 7075 anode both improved with this approach. The corrosion inhibition mechanism and discharge performance enhancement of the 3D structured Al 7075 anode are also discussed in this work. Additionally, a double-face, flow Al-air battery system (DFAB) architecture was employed for driving a toy helicopter to demonstrate performance. In this work, the 3D structured Al 7075 anode achieved world-class power density (356.8 mWcm^{-2}), specific capacity (2444.9 mAh g^{-1}), and

energy density (2941.8 mWh g^{-1}). The results of this study provide a path for an improved design for AABs with increased power and energy density and improved anode corrosion resistance. The suppression of HER and improvement the discharging current density are contradict tasks. This work addresses them simultaneously by FSP to suppress HER and improve ECSA by laser-introduced 3D structures. The current power density is the top value among all reported values.

2. Results and discussion

2.1. Structural characterization of a 3D Al anode

Fig. 1(a–b) shows the microstructural features of the Al 7075 and FSPed Al 7075 samples. Fig. 1 (a) shows that the typical grain size of the Al 7075 sample is ~20 μm–60 μm. After friction stir processing, the grain size was refined to 2–3 μm, shown in Fig. 1 (b). The FSPed sample was further processed by fs laser to form a 3D structure on the top surface with a line pattern. The top view and cross-section of the sample after laser processing were investigated by a Witec-Alpha 300 optical microscope. Fig. 1 (c) shows the top view of the sample, indicating that the width of the laser cutting groove is around 25 μm. The sample cross-section, as Fig. 1 (d) shows, displays the 3D structure and a depth of 99 μm.

2.2. Electrochemical characterization

2.2.1. Potentiodynamic polarization

The anodic cell reaction involves anodic aluminum dissolution and cathodic water reduction to hydrogen in an alkaline solution [43]. The anodic reaction which is the preferred reaction can be shown with the following equation:

$$Al + 4OH^- \rightarrow Al(OH)_4^- + 3e^- \tag{1}$$

The parasitic reaction on the electrode surface is mainly the reduction of water, i.e.:

$$2H_2O + 2e^- \rightarrow H_2 + 2OH^- \tag{2}$$

The OH$^-$ ions formed by this hydration increase the alkalinity at the interface of film/solution. As a result, dissolution or change of the electrolyte film structure occurs. The combined preferred and parasitic reactions on the electrode surface is:

$$2Al + 2OH^- + 6H_2O \rightarrow 2Al(OH)_4^- + 3H_2 \tag{3}$$
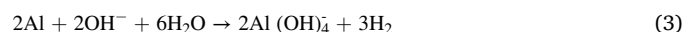
The ideal aluminum anode requires minimizing the electrochemical activity for the secondary reaction, increasing that for the anodic dissolution.

Fig. 2 (a) displays the polarization curves of three aluminum anodes (Al 7075, Al 7075 FSP, 3D Al 7075) in 4 M KOH solutions with a Pt pseudo-reference and graphite counter electrode, and Table S1 gives the corresponding corrosion parameters. The positive overpotential part of polarization curve represents the Al stripping/dissolution, and the negative overpotential part is Al plating/deposition. Both the Al anodes maintain certain activity in a wide potential range and the current increases with overpotential. As the potential is more positive, the limiting currents of anodic dissolution set in, indicating the existence of an oxide film on the surface [44]. It is obvious that the anodic dissolution currents of both the Al 7075 FSP anode and the 3D Al 7075 FSP anode are lower than that of the Al 7075 anode, revealing that the anodic dissolution rates of those two anodes are lower, supporting evidence for the low self-corrosion rate in 4 M KOH solution.

Moreover, the corrosion potential (E$_{corr}$) of the 3D Al 7075 FSP anode is more negative than that of the Al 7075 AND Al 7075 FSP anodes (Table S1), indicating that the 3D Al 7075 FSP anode exhibits a higher electrochemical activity relative to the other two Aluminum anodes [25]. To investigate the more negative corrosion potential of the 3D Al
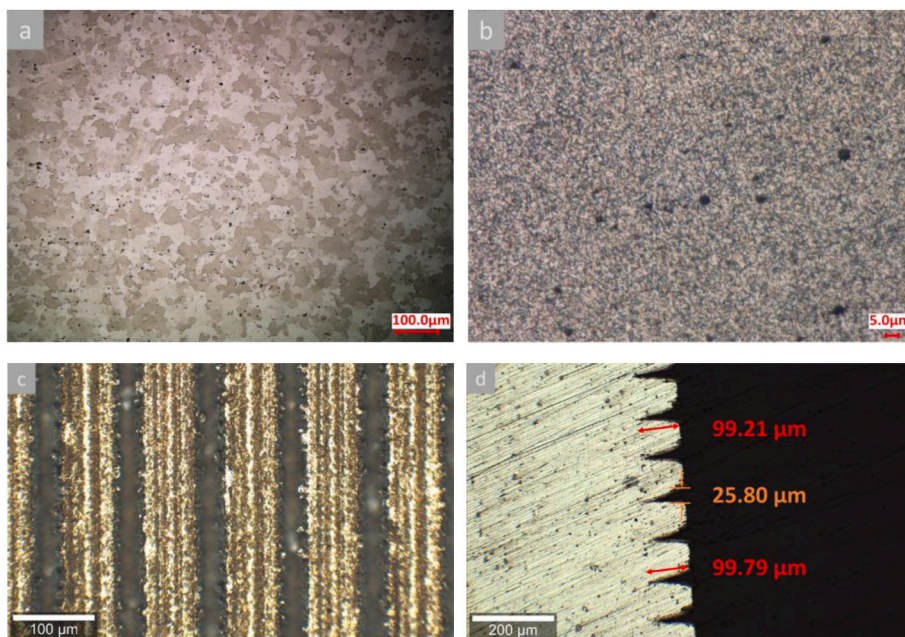
Fig. 1. a: Grain size of Al-7075; b: Grain size of FSPed Al-7075; c (top view) and d (cross-section): Optical microscope photo of FSPed Al-7075 after laser processing.
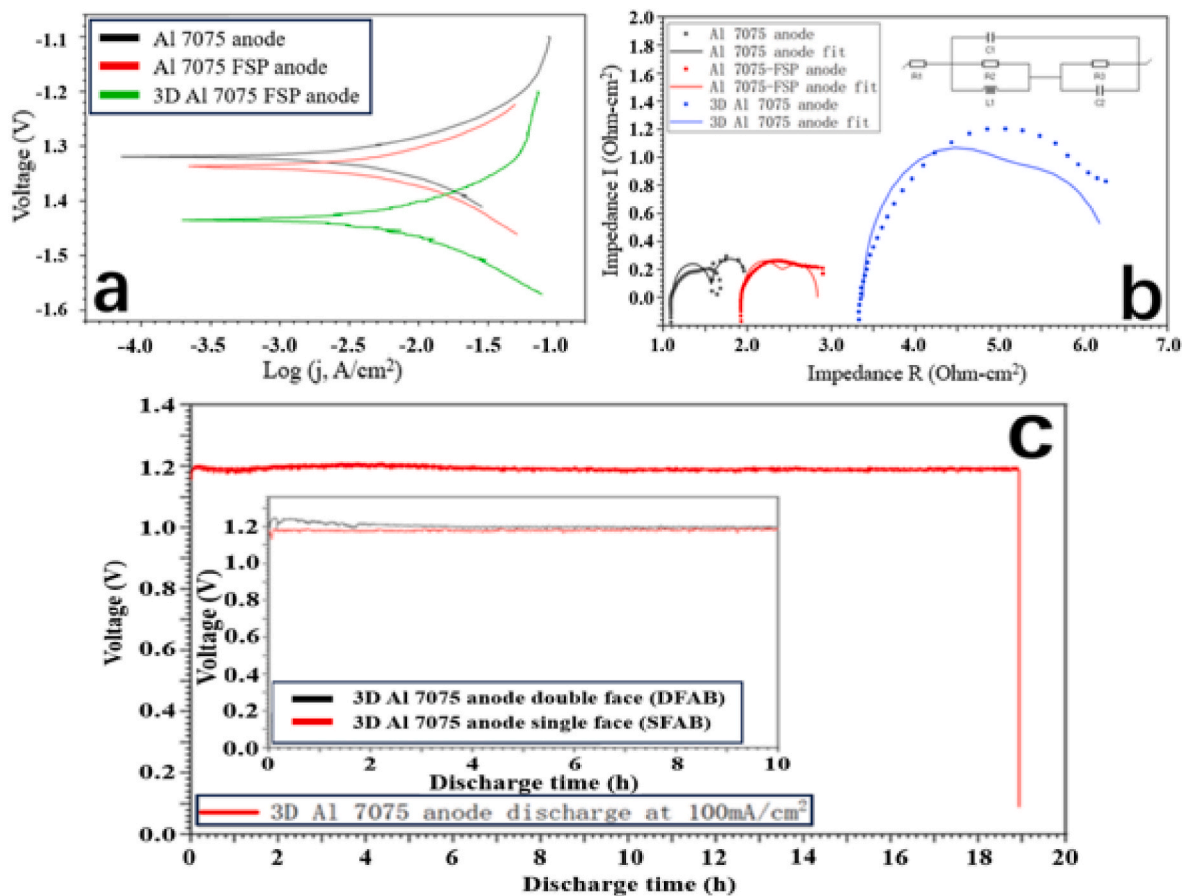

Fig. 2. (a) Potentiodynamic polarization curves for Al7075, FSPed Al 7075 and 3D-FSPed-Al7075 anode samples in 4 M KOH. (b) EIS curves for Al7075, FSPed Al 7075 and 3D-FSPed-Al7075 anode samples in 6 M KOH. (c) Discharge curves of DFAB at 100 mAcm^{-2} for stability. Inset Single face and double face flow Al air battery at 100 mAcm^{-2}, all tests use 3D Al 7075 FSP anode.

7075 FSP anode, we did X-ray fluorescence (XRF) measurements to see whether the laser processing changed the composition within the processed area. According to the XRF results (Table S2), the Al lost nearly 9 % and the percentage of Zn is 9 % higher than the sample before laser processing. Since zinc has a more negative corrosion potential than aluminum [45], the increase of the corrosion after laser process could be explained by a higher Zn fractal after laser irradiation. The 3D Al 7075 FSP anode and Al 7075 FSP anode have a lower J_{corr} value comparable with the Al 7075 anode, which is attributed to the reduction reaction with water (Eq. (2)) by the finer grains [26,27]. The 3D Al 7075 FSP anode displays a high anodic dissolution rate, more negative corrosion potential, and low J_{corr} value, which enhances the performance of the AAB.

2.2.2. Electrochemical impedance spectroscopy (EIS)

Electrochemical impedance spectroscopy (EIS) is used to characterize electrochemical reactions and electrode processes interface [46–49]. Fig. 2 (b) shows the Nyquist plot of three Al anodes in 6 M KOH electrolyte. The Nyquist plots present inductive behavior at high frequency and two capacitive loops at the moderate/lower frequencies. The low frequency capacitive semicircle relates to the oxide film growth on the Al anode surface, and a second capacitive semicircle at higher frequency likely results from the charge transfer process induced by the dissolution of aluminum. The inductive semicircle is believed to be due to the H_2 adsorption in the water reduction reaction [50].

Equivalent circuit analysis with best fit is shown in the top right corner of Fig. 2 (b), and the simulation values of each equivalent element were listed in Table S3. In Fig. 2 (b), R_1 represents the solution resistance. The high frequency capacitive loop represents the charge transfer resistance (R_2) in parallel with a double-layer capacitance (C_1) [25,48]. R_2 reflects the corrosion rate of the anode because the exchange current is directly associated with the electrochemical process of corrosion [48]. Higher R_2 represents lower corrosion rate of Al anode. R_2 increased when the Al 7075 anode was treated by friction-stir process and even higher after fs laser process, indicating that the corrosion rate of Al 7075 FSP and 3D Al 7075 FSP anode was slower than that of commercially available Al 7075 anode. The highest R_2 values obtained for 3D Al 7075 FSP anode may be due to the 3D structure surface morphology. The low frequency capacitive loop corresponds to the complementary Al^+ - Al^{3+} reaction. In the 3D Al 7075 FSP anode, there is hardly a low frequency capacitive loop, indicating that it's more retarded for 3D Al 7075 FSP anode to produce Al^{3+} at a DC condition, which reduces the H_2 generation and qualitatively agrees with other results in this study.

Unlike the geometric surface area, electrochemically active surface area (ECSA) reflects the intrinsic activity of electrode materials. The ECSAs of the three anodes were estimated using a simple cyclic voltammetry (CV) method. Due to the unknown capacitive behavior (C_s) of the Al 7075 alloy, it is difficult to solve the exact surface area. However, relative surface areas of these three samples can be quantified by the double-layer capacitance (C_{dl}). Since the C_{dl} is expected to be linearly proportional to electrochemically active surface area for samples with similar composition, this method has been also employed in previous studies [51–53]. The results of ECSA (Fig. S1) suggested that, due to the 3D structure created by fs laser on the top surface of Al anode, 3D Al 7075 FSP anodes possessed the highest ECSA among all three anodes. Interestingly, the corrosion current density of 3D Al 7075 FSP anode was calculated to be lower than that of the other two (Table S1), indicating for these materials, the impact of increasing the Zn fraction overcame the increase in reactive surface area for enhancing the undesired corrosion reaction. This finding confirms that the construction of 3D structures can reduce Al anode polarization and improve electrochemical reactivities.

2.3. Battery performance

The three aluminum anodes were evaluated by an in-house designed double-face flow Al-air battery system (DFAB). This battery system consisted of an Al alloy plate anode, two catalyst-loaded carbon fiber paper (CFP) air cathodes, and a double-face body with continuous electrolyte supplied from electrolyte tanks by peristaltic pumps, as shown in Fig. S2. The advantage of the flow battery design, compared with the static battery, is that the by-product deposition on the surface of cathode can be fully avoided. For the static battery, even using a 3D electrode, the pores and canals of the cathode were clogged by reaction product deposition, leading to rapid loss of three-phase reaction interfaces and elimination of cathodic reaction. Conversely, when the DFAB was running, fresh electrolyte constantly washed off precipitating solid by-products ($Al(OH)_3$, Al_2O_3), keeping the reactive surface area of the cathode clean [54], greatly extending useable lifetime. This was also demonstrated by the discharge performance of the DFAB at 100 $mAcm^{-2}$ using 3D Al 7075 FSP anode (Fig. 2 (c)). The DFAB discharge lasted nearly 19 h without showing significant voltage loss until the testing was terminated by choice. The 3D structure was observed fully reactivated after discharge, which indicates a high utilization of the anode by the DFAB design. The discharge performance of the single-face and the double-face flow AABs at 100 $mAcm^{-2}$ was evaluated by using 3D Al 7075 FSP anode. The inset of Fig. 2(c) shows their discharge voltages were both ~1.2 V, meaning the double-face structure did not negatively impact the discharge process of the flow battery.

Using this DFAB design, we compared the practical performance of the 3D Al 7075 anode with Al 7075 FSP anode and Al 7075 anode. As seen in Fig. 3 (a), the discharge voltage of 3D Al 7075 anode is higher than both Al 7075 FSP anode and Al 7075 anode at the same current, and throughout the entire polarization curve. Fig. 3 (b) shows that the maximum power density of 3D Al 7075 FSP anode reached ~ 337.8 $mWcm^{-2}$ at 464.1 $mAcm^{-2}$, which was much higher than that of Al 7075 anode (~194.1 $mWcm^{-2}$ at 297.1 $mAcm^{-2}$) and Al 7075 FSP anode (~276.3 $mWcm^{-2}$ at 404.4 $mAcm^{-2}$), revealing that 3D Al 7075 FSP anode demonstrated better practical discharge performance at high current density. As shown in Fig. 3 (c), a voltage of 0.76 V was obtained at 400 $mAcm^{-2}$ for 3D Al 7075 FSP anode, which significantly exceeded the Al 7075 anode. This result also supports the conclusion that 3D Al 7075 FSP anode performed better at higher current density with little evidence of mass transport limitation.

The specific capacity and energy of all the three different Al anodes were assessed by galvanostatic discharge tests at 100 $mAcm^{-2}$. As summarized in Table 1, the mass specific capacity and the mass energy density of 3D Al 7075 FSP anode were 2445 $mAh\ g^{-1}$ and 2942 $mWh\ g^{-1}$, higher than those of the Al 7075 anode (2179 $mAh\ g^{-1}$ and 2257 $mWh\ g^{-1}$) and Al 7075 FSP anode (2396 $mAh\ g^{-1}$ and 2575 $mWh\ g^{-1}$). The high energy and power density of 3D Al 7075 anode compared to the others tested was a result of the combination of enhanced corrosion resistance from the FSP treatment and increased ECSA from the laser treatment.

2.4. Discussion

The microstructures of the Al 7075 anode, Al 7075 FSP anode, and 3D Al 7075 FSP anode were further analyzed by Electron Backscatter Diffraction (EBSD). As the EBSD inverse pole figure (IPF) maps show in Fig. 4 (a) and (b), the Al 7075 anode exhibits elongated grains while the Al 7075 FSP anode is comprised of fine, equiaxial grains with uniform size distribution. Fig. 4 (d) and (e) illustrate the grain size distribution statistical histograms of Al 7075 and Al 7075 FSP anodes; the average grain size was 33.9 μm and 2.2 μm, respectively (calculated by the EDAX OIM Analysis software). Fig. 4 (g) and (h) illustrate the grain boundary misorientation of the Al 7075 and Al 7075 FSP anodes. Low angle grain boundaries (LAGBs) with misorientations of smaller than 15° and high angle grain boundaries (HAGBs) with misorientations larger than 15°
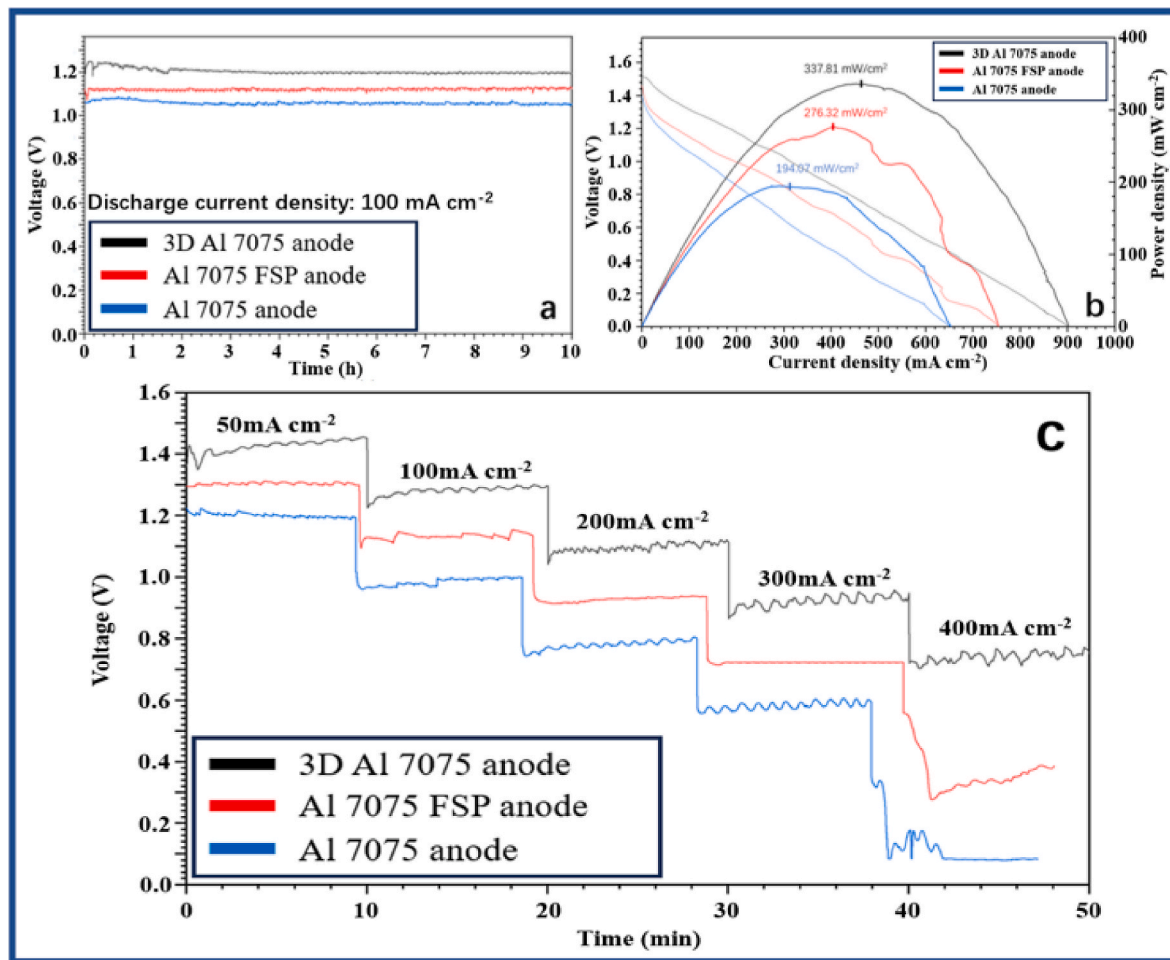
Fig. 3. DFAB battery performance. a) discharge curves of three Al anodes at 100 mAcm^{-2}; b) polarization and power density curve of three Al anodes; c) discharge curves of the three Al anodes by using DFAB at different discharging current densities.

Table 1
Summary of electrochemical performance of the DFAB for three anodes.

Sample	Al 7075 anode	Al 7075 FSP	3D Al 7075 FSP
Current density (mA cm^{-2})	100	100	100
Specific capacity (mAh g^{-1})	2179	2396	2445
Energy density (mWh g^{-1})	2257	2575	2942

are shown in the subfigure in Fig. 4 (i). It is evident that the equiaxial grains in the Al 7075 FSP anode display a large fraction of HAGBs (59.6 %) while the commercially available Al 7075 anode mostly had LAGBs. According to Zhang et al. [55], it is believed that the grain boundary misorientation dependency of intergranular corrosion susceptibility in the Al alloy is mainly due to the difference in grain boundary energy that is determined by the degree of misfit between atoms across the boundary, generally grain boundary misorientation. Since grain boundary misorientation facilitates intergranular corrosion, and the HAGBs with high grain boundary energy display higher susceptibility to intergranular corrosion than LAGBs. However, grain size and distribution also affect the corrosion resistance of Al anode [56,57]. According to our result, the grain size is one order of magnitude smaller than the unmodified 7075, which could lead the corrosion resistance significantly improved; in that case, the corrosion resistance is increased although it possesses a higher percentage of high angle grain boundaries (HAGBs) with higher susceptibility to intergranular corrosion.

Fig. 4 (c) shows the IPF figure of 3D Al 7075 FSP anode for area near the laser ablated zone while the black area indicates the groove created

by the fs laser. Near the laser ablation area (with a depth of around 20 μm), the average grain size was 1.32 μm, which is even smaller than that of the FSP Al 7075 anode. The finer grains around the laser ablation area were probably formed due to the grain refinement effect of the fs laser peening [58]. The grain boundary misorientation of 3D Al 7075 FSP anode shown in Fig. 4 (i) illustrates that the percentage of LAGBs (52.4 %) is higher than FSP Al 7075 anode (40.3 %). Based on the anti-corrosive effect of both LAGBs and finer grain sizes, the higher corrosion resistance of 3D Al 7075 FSP anode is supported.

X-ray photoelectron spectroscopy (XPS) was used to investigate elemental information before and after fs laser processing. The XPS survey spectra of 3D Al 7075 FSP anode and FSP Al 7075 anode are plotted in Fig. 5 (a). It is apparent that the peaks in these survey spectra include C 1s and O 1s, which could be due to the sample surface contamination and oxidation during transportation. Fig. 5(b–d) shows the high-resolution Al 2p, Mg 2s, and Zn 2p lines. It is obvious that, after fs laser processing, the responses for Zn 2p and Mg 2s became more visible. The atomic percentages of Al, Mg and Zn are 71.2 %, 6.5 %, 22.2 % for 3D Al 7075 FSP anode, and 80.5 %, 4.1 %, 15.3 % for Al 7075 FSP anode, respectively. These results are consistent with the XRF measurements: after fs laser processing, the Al elemental percentage among 3D Al 7075 FSP anode surface decreased and elements with higher corrosion potentials (Mg, Zn) increased. At the current stage, it is unclear why Zn is enriched after laser processing. It is possible that Zn forms a stable phase which has a lower rate of laser ablation. It is noting that Zn forms MgZn$_2$ precipitates at 350 °C in Al7075 [59]. Different ablation rates between Al and MgZn$_2$ may result in a relative high Zn.
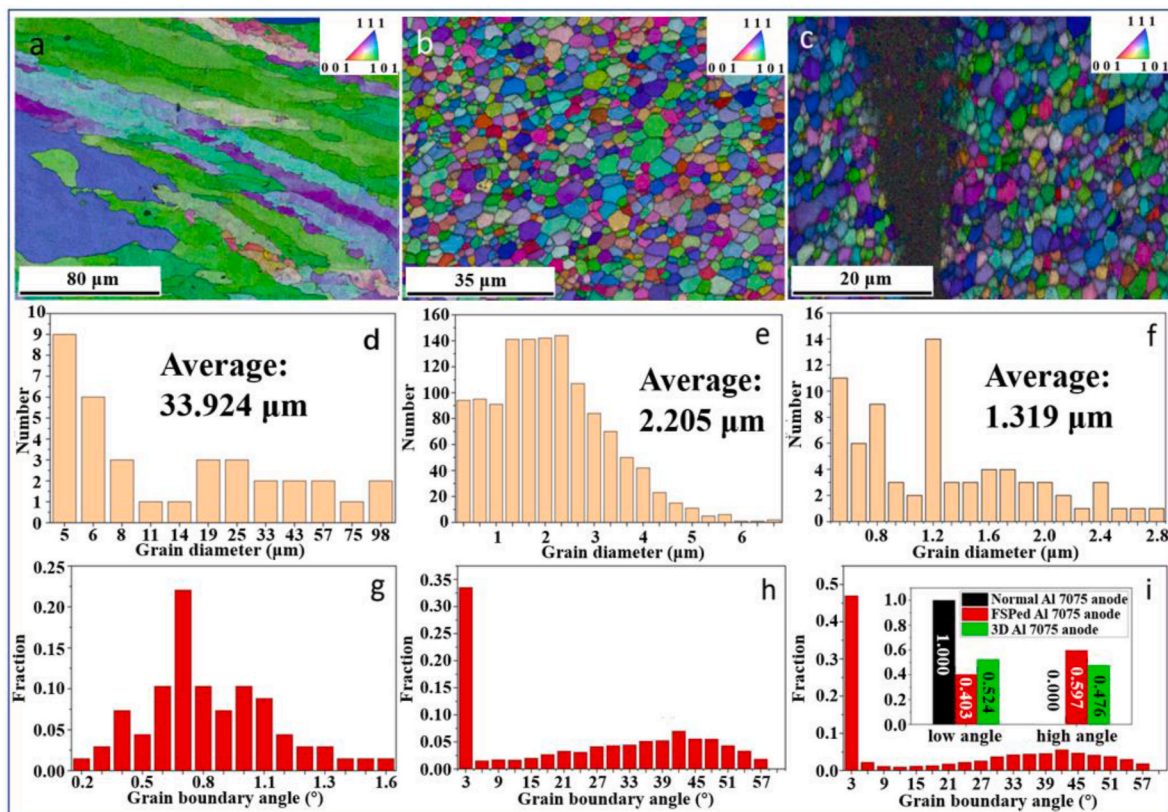
Fig. 4. EBSD inverse pole figure (IPF) maps, grain size statistical histogram and grain misorientation statistical histogram of Al 7075 anode (a, d, g), Al 7075 FSP anode (b, e, h), and 3D Al 7075 FSP anode (c, f, i).
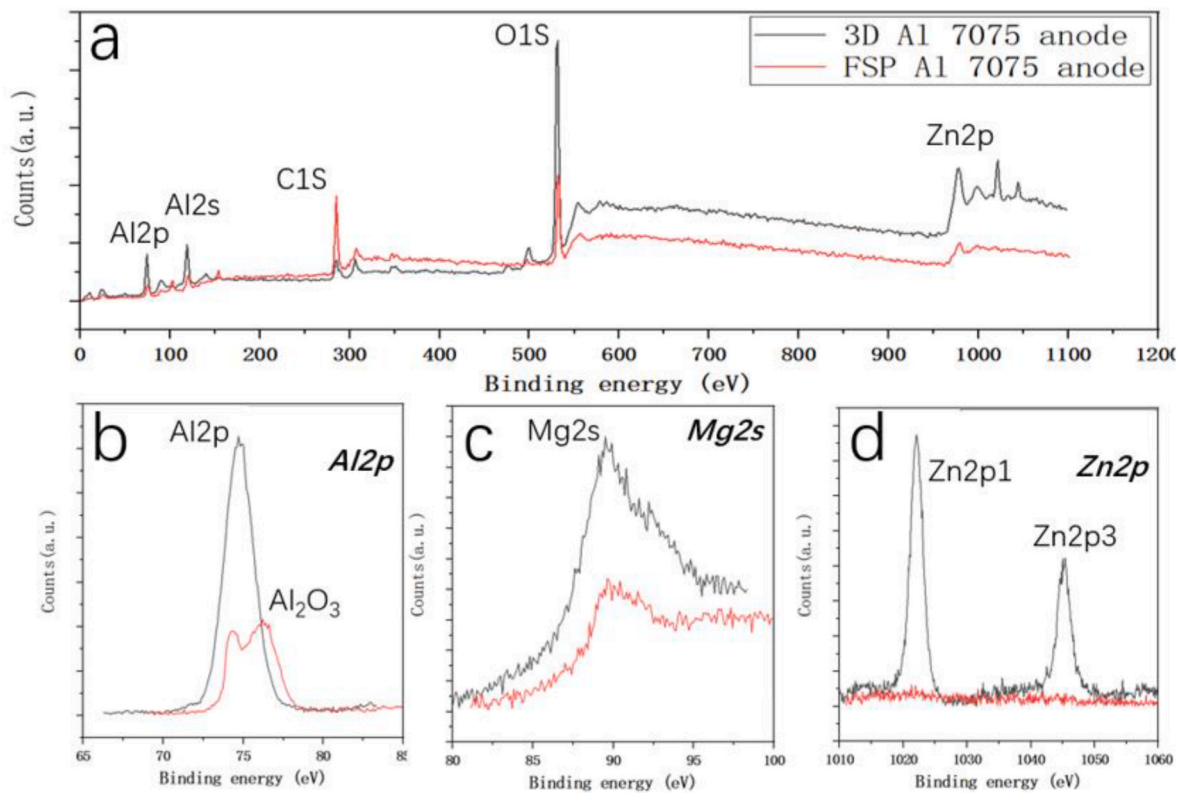

Fig. 5. (a) XPS survey spectra of the surfaces obtained 3D Al 7075 FSP anode and FSP Al 7075 anode. (b), (c) and (d) are the high-resolution Al2p, Mg2s and Zn2p core level XPS spectra, respectively. The legend from figure an applied for all figures (a–d).

However, further work needs to elucidate the reason for Zn enrichment. Anyway, these composition changes result in a higher corrosion resistance of the 3D Al 7075 FSP anode surface.

Table S4 lists typical Al – air battery performance reported by other groups in recent years. It is shown that the 3D Al 7075 FSP anode reached the highest power density (337.8 mWcm^{-2}) and is comparable to both the best specific capacity and energy density. The practical performance of the battery is also demonstrated by driving a helicopter model (3.7 V, 1 A, see video in Supplementary Movie S1), which further demonstrates the excellent battery performance.

3. Conclusions

In conclusion, 3D Al 7075 FSP anode was prepared by a two-step process. The grain size was refined by the friction-stir process and the surface area was improved significantly by the fs laser engineering. In comparison to the unmodified Al 7075 anode and Al 7075 FSP anode, 3D Al 7075 FSP anode achieved higher power density (337 mWcm^{-2}) at a high current of 464 mAcm^{-2}, which was among the best reported results found by the authors in current literature. The 3D Al 7075 FSP anode also exhibited better electrocatalytic performance (discharge voltage of 0.76 V at 400 mAcm^{-2}, energy density of 2941 mWh g^{-1}, and specific capacity of 2445 mAh g^{-1}) than that of the normal Al 7075 anode. This work verified that micro-nano structured 3D Al anodes using fs laser engineering and friction-stir processing are an efficient strategy for improving the battery discharge voltage and current, which can be significant to the commercialization of AAB. Further studies will focus on the effect of adding other elements through friction-stir process and elucidating composite variation due to laser processing. We believe these can further optimize the efficiency of the Al-air battery.

4. Methods

4.1. Preparation of 3D Al 7075 FSP anodes

A commercial 120 mm × 80 mm × 6 mm Al 7075 plate was subjected to the single-pass friction stir processing (FSP) using MTS ISTIR friction stir welding machine with a rotation rate of 550 rpm and traveling speed of 25.4 mm/min [60]. The stir tool was made of H13 tool steel. The diameter of the scrolled shoulder and threaded pin was 19 mm and 6.3 mm, respectively, while the length of the pin was 4.7 mm.

The FSPed sample was cut into pieces (20 mm × 20 mm) and the surface was polished with 1200 grit sandpaper. Then the 3D structure of the top surface of FSPed sample was fabricated by a fs laser (model: Amplitude-Tangor SY4973) with a repetition rate of 10 kHz, a wavelength of 1030 nm, and the pulse duration of 500 fs. The factor influences the width of the groove includes the sample moving speed, the focus of laser beam and the laser power. The diameter of the focused laser beam was 3 μm and the processing power was 1.5 W. A line-by-line printing pattern was used with a line interval of 100 μm and sample moving speed of 1 mm/s in both X and Y axes. The schematic of the whole process is shown in Fig. S3. To test if the printing pattern affected the result, results for other laser patterns (dot pattern and crossbar pattern) are shown in Fig. S4.

Alloys of Al 7005 and Al 1000 (minimum of 99 % aluminum, no major alloying additions) were also tested for specific capacity; the results in Table S5 verify that Al 7075 has higher specific capacity and better corrosion resistance. As a result, this alloy was used for the studies in this work. The main challenge of the friction stir processing is the micro-crack generation during the process, which could lead to a drop of battery performance. For the laser processing, the limitation appeared to be the focus of the laser beam onto the surface of the sample and how to make the groove deeper and narrower so that the surface area could be increasing more. Those issues will be the next step of the research plan in order to further increase the efficiency of the battery.

4.2. Preparation of MnOOH–CeO$_2$ carbon fiber paper cathode

MnOOH–CeO$_2$ nanowires were prepared by a hydrothermal method [13]. 300 mg of KMnO$_4$ and 9 mg of Ce(NO$_3$)$_3$·6H$_2$O were dissolved in 30 mL 5 vol% aqueous ethanol solution and transferred to a Teflon-lined autoclave. Then, the autoclave was sealed and held at 120 °C for 12 h. The resultant was filtered and washed with DI water and ethanol several times and then dried at 60 °C in an oven for 12 h.

The MnOOH–CeO$_2$ cathode was fabricated by an electrophoretic deposition (EPD) method [61]. Carbon fiber papers (CFP, model-TGP-H-060) serving as the cathode were ultrasonically cleaned with ethanol and dried. Afterwards, a graphite electrode accompanied with the clean CFP (1 cm × 1 cm) was inserted vertically into the electrolyte with a constant distance of ~1.0 cm from cathode. The electrolyte contained ethanol and acetylacetone (volume ratio of 1:1) with sodium dodecyl sulfate (SDS, 0.0025 M) as additive. The concentration of MnOOH–CeO$_2$ nanowire in the electrolyte was 0.5 g/L. The applied voltage, current, and deposition time were 100 V, 0.05 A and 5 min, respectively. After the EPD process, the carbon fiber paper was dried at 60 °C in the dryer for 2 h, and then 2 mL carbon-solution (Ketjen Black (KB), Super-P mixed with weight ratio 3:1, and then added into pure ethanol at a concentration of 1 mg/mL) was dripped slowly onto the CFP to enhance electronic conductivity.

4.3. Electrochemical characterizations

Potentiodynamic polarization curves, electrochemical impedance spectroscopy (EIS) and electrochemical active surface area (ECSA) characterization were carried out with a three-electrode system at room temperature (~25 °C) by an electrochemical workstation (model: Biologic-SP200). A Pt electrode served as the reference electrode and a 1 cm × 1 cm graphite sheet was used as the counter electrode. The solution used in this study was 6 M KOH. The samples were ground and polished with 1200 grit sandpaper and then washed with ethanol. The working electrode open circuit potential (OCP) was measured with an exposed area of 1 cm^2. Before electrochemical examination, the specimens were submerged in the test electrolyte for 30 min to make sure the OCP was constant. The potentiodynamic polarization was measured with the linear sweep voltammetry in a range of +500 ~ −500 mV (vs. OCP) with a 0.1 mV s^{-1} scanning rate. The EIS measurement was carried out at OCP with a 10 mV sine perturbation in the frequency range of 100 kHz - 0.1 Hz; equivalent circuit models were fitted by EC-Lab software.

5. Design and assembly of aluminum-air double-side flow cells

The practical performance of as-prepared samples was investigated using a battery testing system by a self-made double-face flow Al-air battery (DFAB) system, which contained our 3D Al 7075 aluminum alloy anode, a MnOOH–CeO$_2$ CFP cathode and alkaline aqueous electrolyte with corrosion inhibitors. The alkaline aqueous electrolyte included 6 M KOH with inhibitors (0.01 M Na$_2$SnO$_3$, 0.0075 M ZnO, 0.0005 M In(OH)$_3$). The schematic of the whole DFAB design was presented in Fig. S2. Comparing with single face flow Al-air battery, the DFAB system consisted of an Al alloy plate anode and two catalyst-loaded air cathodes, which enabled DFAB a larger discharge current than the normal single-face battery without adding too much volume. The detailed calculations of DFAB testing data were explained in the Supplementary Materials.

CRediT authorship contribution statement

Lingyue Zhang: Conceptualization, Methodology, Data curation, Writing – original draft, Writing – review & editing. **David Fieser:** Data curation, Writing – review & editing. **Bapi Bera:** Methodology, Writing – review & editing. **Douglas Aaron:** Resources, Methodology, Writing – review & editing. **Matthew M. Mench:** Resources, Writing – review &

editing. **Anming Hu:** Conceptualization, Data curation, Resources, Writing – review & editing, Supervision, Project administration. **Yuan Li:** Methodology, Data curation, Writing – review & editing. **Jian Chen:** Resources, Writing – review & editing. **Zhili Feng:** Resources, Writing – review & editing. **Antonino Gulino:** Resources, Writing – review & editing. **Giuseppe Compagnini:** Resources, Writing – review & editing.

Declaration of competing interest

The authors declare that they have no known competing financial interests or personal relationships that could have appeared to influence the work reported in this paper.

Data availability

Data will be made available on request.

Acknowledgement

Appendix A. Supplementary data

Supplementary data to this article can be found online at https://doi.org/10.1016/j.jpowsour.2023.233752.

References

[1] M. Park, J. Ryu, W. Wang, J. Cho, Material design and engineering of next-generation flow-battery technologies, Nat. Rev. Mater. 2 (1) (2016) 1–18.

[2] W. Yu, W. Shang, P. Tan, B. Chen, Z. Wu, H. Xu, Z. Shao, M. Liu, M. Ni, Toward a new generation of low cost, efficient, and durable metal-air flow batteries, J. Mater. Chem. A 7 (47) (2019) 26744–26768.

[3] [3a] Z.J. Zhang, Z.Z. Yao, S.C. Xiang, B.L. Chen, Energy Environ. Sci. 7 (2011) 2868–2899, 2014.[3]b)B. Dunn, H. Kamath, J.-M. Tarascon. Science, 334, 928-935..

[4] T. Liu, J.P. Vivek, E.W. Zhao, J. Lei, N. Garcia-Araez, C.P. Grey, Current challenges and routes forward for nonaqueous lithium–air batteries, Chem. Rev. 120 (14) (2020) 6558–6625.

[5] S. Yang, Y. Cheng, X. Xiao, H. Pang, Development and application of carbon fiber in batteries, Chem. Eng. J. 384 (2020), 123294.

[6] H. Yang, H. Li, J. Li, Z. Sun, K. He, H.M. Cheng, F. Li, The rechargeable aluminum battery: opportunities and challenges, Angew. Chem. Int. Ed. 58 (35) (2019) 11978–11996.

[7] M. Mokhtar, M.Z.M. Talib, E.H. Majlan, S.M. Tasirin, W.M.F.W. Ramli, W.R. W. Daud, J. Sahari, Recent developments in materials for aluminum–air batteries: a review, J. Ind. Eng. Chem. 32 (2015) 1–20.

[8] Hao Jiang, Jinxing Gu, Xusheng Zheng, Min Liu, Xiaoqing Qiu, Liangbing Wang, Wenzhang Li, Zhongfang Chen, Xiaobo Ji, Jie Li, Defect-rich and ultrathin N doped carbon nanosheets as advanced trifunctional metal-free electrocatalysts for the ORR, OER and HER, Energy Environ. Sci. 12 (no. 1) (2019) 322–333.

[9] Y. Wang, H.Y. Kwok, W. Pan, Y. Zhang, H. Zhang, X. Lu, D.Y. Leung, Combining Al-air batteries with paper-making industry, a novel type of flexible primary battery technology, Electrochim. Acta 319 (2019) 947–957.

[10] H. Wang, D.Y. Leung, M.K. Leung, Energy analysis of hydrogen and electricity production from aluminum-based processes, Appl. Energy 90 (1) (2012) 100–105.

[11] Y. Liu, Q. Sun, W. Li, K.R. Adair, J. Li, X. Sun, A comprehensive review on recent progress in aluminum–air batteries, Green Energy Environ. 2 (3) (2017) 246–277.

[12] Y. Ma, A. Sumboja, W. Zang, S. Yin, S. Wang, S.J. Pennycook, Z. Kou, Z. Liu, X. Li, J. Wang, Flexible and wearable all-solid-state Al-air battery based on iron carbide encapsulated in electrospun porous carbon nanofibers, ACS Appl. Mater. Interfaces 11 (2) (2019 Jan 16) 1988–1995.

[13] Depei Liu, Jing Tian, Yougen Tang, Jingsha Li, Shijie Yi, Xiaobing Huang, Dan Sun, Haiyan Wang, High-power double-face flow Al-air battery enabled by CeO2 decorated MnOOH nanorods catalyst, Chem. Eng. J. 406 (2021), 126772.

[14] Y. Wang, H. Kwok, W. Pan, H. Zhang, D.Y. Leung, Innovative paper-based Al-air batteries as a low-cost and green energy technology for the miniwatt market, J. Power Sources 414 (2019) 278–282.

[15] Depei Liu, Liang Fu, Xiaobing Huang, Kun Liu, Jingsha Li, Hualin Xie, Haiyan Wang, Yougen Tang, Influence of iron source type on the electrocatalytic activity toward oxygen reduction reaction in Fe-N/C for Al-air batteries, J. Electrochem. Soc. 165 (9) (2018) F662.

[16] J. Ryu, H. Jang, J. Park, Y. Yoo, M. Park, J. Cho, Seed-mediated atomic-scale reconstruction of silver manganate nanoplates for oxygen reduction towards high-energy aluminum-air flow batteries, Nat. Commun. 9 (1) (2018) 3715.

[17] J. Wang, A. Wu, Z. Qiu, A. Li, W. Qin, H. Huang, N-CNT supported Fe/Ce bimetallic catalyst for Al-air aqueous batteries, Appl. Surf. Sci. 608 (2023), 155185.

[18] S. Sun, Y. Xue, Q. Wang, H. Huang, H. Miao, Z. Liu, Cerium ion intercalated MnO2 nanospheres with high catalytic activity toward oxygen reduction reaction for aluminum-air batteries, Electrochemical Acta 263 (2018) 544–554.

[19] H. Huang, P. Liu, Q. Ma, Z. Tang, M. Wang, J. Hu, Airborne ultrasound catalyzed saltwater Al/Mg-air flow batteries, Energy 270 (2023), 126991.

[20] Hejing Wen, Zhongsheng Liu, Qiao Jia, Ronghua Chen, Ruijie Zhao, Jianchun Wu, Guanjun Qiao, Jianhong Yang, High energy efficiency and high power density aluminum-air flow battery, Int. J. Energy Res. 44 (9) (2020) 7568–7579.

[21] B.J. Hopkins, Y. Shao-Horn, D.P. Hart, Suppressing corrosion in primary aluminum–air batteries via oil displacement, Science 362 (6415) (2018) 658–661.

[22] J. Ma, J. Wen, J. Gao, Q. Li, Performance of Al–0.5 Mg–0.02 Ga–0.1 Sn–0.5 Mn as anode for Al–air battery in NaCl solutions, J. Power Sources 253 (2014) 419–423.

[23] Chunlian Wang, Yongchao Yu, Jiajia Niu, Yaxuan Liu, Denzel Bridges, Xianqiang Liu, Pooran Joshi, Yuefei Zhang, Anming Hu, Recent progress of metal–air batteries—a mini review, Appl. Sci. 9 (14) (2019) 2787.

[24] Y. Han, J. Ren, C. Fu, M. Jiang, S. Lu, J. Zhang, B. Sun, Electrochemical performance of aluminum anodes with different grain sizes for Al-air batteries, J. Electrochem. Soc. 167 (4) (2020), 040514.

[25] L. Fan, H. Lu, The effect of grain size on aluminum anodes for Al–air batteries in alkaline electrolytes, J. Power Sources 284 (2015) 409–415.

[26] Xiaobo Zheng, Ting Zhang, Hejie Yang, Qiaoling Zheng, Yimin Gao, Zhiwei Liu, Wen Wang, Kuaishe Wang, Friction stir processing induced elctrochemical performance improvement of commercial Al for Al-air battery, Electrochim. Acta 354 (2020), 136635.

[27] S. Linjee, S. Moonngam, P. Klomjit, N.S. Pålsson, C. Banjongprasert, Corrosion behaviour improvement from the ultrafine-grained Al–Zn–In alloys in Al–air battery, Energy Rep. 8 (2022) 5117–5128.

[28] S. Gollapudi, Grain size distribution effects on the corrosion behaviour of materials, Corrosion Sci. 62 (2012) 90–94.

[29] J.J. Pang, F.C. Liu, J. Liu, M.J. Tan, D.J. Blackwood, Friction stir processing of aluminium alloy AA7075: microstructure, surface chemistry and corrosion resistance, Corrosion Sci. 106 (2016) 217–228.

[30] T.S. Mahmoud, Effect of friction stir processing on electrical conductivity and corrosion resistance of AA6063-T6 Al alloy, Proc. IME C J. Mech. Eng. Sci. 222 (7) (2008) 1117–1123.

[31] Min Jiang, Chaopeng Fu, Pengyu Meng, Jianming Ren, Jing Wang, Junfu Bu, Anping Dong, Jiao Zhang, Wei Xiao, Baode Sun, Challenges and strategies of low-cost aluminum anodes for high-performance Al-based batteries, Adv. Mater. 34 (2) (2022), 2102026.

[32] D.R. Egan, C.P. De León, R.J.K. Wood, R.L. Jones, K.R. Stokes, F.C. Walsh, Developments in electrode materials and electrolytes for aluminum–air batteries, J. Power Sources 236 (2013) 293–310.

[33] C. Li, W. Ji, J. Chen, Z. Tao, Metallic aluminum nanorods: synthesis via vapor-deposition and applications in Al/air batteries, Chem. Mater. 19 (24) (2007) 5812–5814.

[34] Y. Yu, M. Chen, S. Wang, C. Hill, P. Joshi, T. Kuruganti, A. Hu, Laser sintering of printed anodes for al-air batteries, J. Electrochem. Soc. 165 (3) (2018) A584.

[35] Y. Xu, Y. Zhao, J. Ren, Y. Zhang, H. Peng, An all-solid-state fiber-shaped aluminum–air battery with flexibility, stretchability, and high electrochemical performance, Angew. Chem. 128 (28) (2016) 8111–8114.

[36] Z. Zhang, C. Zuo, Z. Liu, Y. Yu, Y. Zuo, Y. Song, All-solid-state Al–air batteries with polymer alkaline gel electrolyte, J. Power Sources 251 (2014) 470–475.

[37] S. Yu, X. Yang, Y. Liu, F. Zhan, Q. Wen, J. Li, W. Li, High power density Al-air batteries with commercial three-dimensional aluminum foam anode, Ionics 26 (2020) 5045–5054.

[38] U. Rist, V. Falkowski, W. Pfleging, Electrochemical properties of laser-printed multilayer anodes for lithium-ion batteries, Nanomaterials 13 (17) (2023) 2411.

[39] Y. Wang, L. Cao, S. Li, J. Xu, R. Xiao, T. Huang, Effect of laser-textured Cu foil with deep ablation on Si anode performance in Li-ion batteries, Nanomaterials 13 (18) (2023) 2534.

[40] Fabrication of Micron-Sized Protrusions on Metal Surface for Metal Polymer Easy-Disassembly Joining by Selective Laser Melting Technology.

[41] X. Fu, G. Jiang, G. Wen, R. Gao, S. Li, M. Li, J. Zhu, Y. Zheng, Z. Li, Y. Hu, L. Yang, Densely accessible Fe-Nx active sites decorated mesoporous-carbon-spheres for oxygen reduction towards high performance aluminum-air flow batteries, Appl. Catal. B Environ. 293 (2021), 120176.

[42] H. Wen, Z. Liu, J. Qiao, R. Chen, R. Zhao, J. Wu, G. Qiao, J. Yang, High energy efficiency and high-power density aluminum-air flow battery, Int. J. Energy Res. 44 (9) (2020) 7568–7579.

[43] M.A. Rahman, X. Wang, C. Wen, High energy density metal-air batteries: a review, J. Electrochem. Soc. 160 (10) (2013) A1759.

[44] J.B. Wang, J.M. Wang, H.B. Shao, J.Q. Zhang, C.N. Cao, The corrosion and electrochemical behaviour of pure aluminium in alkaline methanol solutions, J. Appl. Electrochem. 37 (2007) 753–758.

[45] Y. Tang, L. Lu, H.W. Roesky, L. Wang, B. Huang, The effect of zinc on the aluminum anode of the aluminum–air battery, J. Power Sources 138 (1–2) (2004) 313–318.

[46] J. Ma, J. Wen, J. Gao, Q. Li, Performance of Al− 1Mg− 1Zn− 0.1 Ga− 0.1 Sn as anode for Al-air battery, Electrochim. Acta 129 (2014) 69–75.

[47] Chenyu Zhu, Yuanyuan Ma, Wenjie Zang, Cao Guan, Ximeng Liu, Stephen J. Pennycook, John Wang, Wei Huang, Conformal dispersed cobalt nanoparticles in hollow carbon nanotube arrays for flexible Zn-air and Al-air batteries, Chem. Eng. J. 369 (2019) 988–995.

[48] Z. Sun, H. Lu, Performance of Al-0.5 in as anode for Al–air battery in inhibited alkaline solutions, J. Electrochem. Soc. 162 (8) (2015) A1617.

[49] T.M. Di Palma, F. Migliardini, D. Caputo, P. Corbo, Xanthan and κ-carrageenan based alkaline hydrogels as electrolytes for Al/air batteries, Carbohydr. Polym. 157 (2017) 122–127.

[50] B. Hirschorn, M.E. Orazem, B. Tribollet, V. Vivier, I. Frateur, M. Musiani, Determination of effective capacitance and film thickness from constant-phase-element parameters, Electrochim. Acta 55 (21) (2010) 6218–6227.

[51] Chunshuang Yan, Chade Lv, Bei-Er Jia, Lixiang Zhong, Xun Cao, Xuelin Guo, Hengjie Liu, et al., Reversible Al metal anodes enabled by amorphization for aqueous aluminum batteries, J. Am. Chem. Soc. 144 (25) (2022) 11444–11455.

[52] M.A. Lukowski, A.S. Daniel, F. Meng, A. Forticaux, L. Li, S. Jin, Enhanced hydrogen evolution catalysis from chemically exfoliated metallic MoS2 nanosheets, J. Am. Chem. Soc. 135 (28) (2013) 10274–10277.

[53] J. Su, Y. Yang, G. Xia, J. Chen, P. Jiang, Q. Chen, Ruthenium-cobalt nanoalloys encapsulated in nitrogen-doped graphene as active electrocatalysts for producing hydrogen in alkaline media, Nat. Commun. 8 (1) (2017), 14969.

[54] N. Zhang, C. Deng, S. Tao, L. Guo, Y. Cheng, Bifunctional oxygen electrodes with gradient hydrophilic/hydrophobic reactive interfaces for metal air flow batteries, Chem. Eng. Sci. 224 (2020), 115795.

[55] X. Zhang, Y. Lv, T. Hashimoto, J.O. Nilsson, X. Zhou, Intergranular corrosion of AA6082 Al–Mg–Si alloy extrusion: the influence of trace Cu and grain boundary misorientation, J. Alloys Compd. 853 (2021), 157228.

[56] C. Berlanga-Labari, M.V. Biezma-Moraleda, P.J. Rivero, Corrosion of cast aluminum alloys: a review, Metals 10 (10) (2020) 1384.

[57] V. Patel, W. Li, A. Vairis, V. Badheka, Recent development in friction stir processing as a solid-state grain refinement technique: microstructural evolution and property enhancement, Crit. Rev. Solid State Mater. Sci. 44 (5) (2019) 378–426.

[58] Anming Hu (Ed.), Laser Micro-nano-manufacturing and 3D Microprinting, Springer, Berlin/Heidelberg, Germany, 2020.

[59] J.A. Wert, Identification of precipitates in 7075 Al after high temperature aging, Script Matal 15 (1981) 445.

[60] S. Zhang, A. Frederick, Y. Wang, M. Eller, P. McGinn, A. Hu, Z. Feng, Microstructure evolution and mechanical property characterization of 6063 aluminum alloy tubes processed with friction stir back extrusion, JOM 71 (2019) 4436–4444.

[61] J. Wu, S. Xue, D. Bridges, Y. Yu, C. Smith, J. Hong, C. Hill, Z. Zhang, F. Feng, A. Hu, Electrophoretic deposition and thermo-chemical properties of Al/Fe2O3 nanothermite thick films, Engineered Science 4 (2) (2018) 52–64.